Simultaneous Focused Electron Beam Induced Deposition and Etching in UHV with Ru(CO)$_4$I$_2$ as Precursor

Elif Bilgilisoy[a], Jo-Chi Yu[b], Christian Preischl[a], Lisa McElwee-White[b], Hans-Peter Steinrück[a*], and Hubertus Marbach[a,c*]

[a] Physikalische Chemie II, Friedrich-Alexander Universität Erlangen-Nürnberg, 91058 Erlangen, Germany

[b] Department of Chemistry, University of Florida, Gainesville, FL 32611-7200, USA

[c] Carl Zeiss SMT GmbH, 64380 Roßdorf, Germany

*Corresponding authors: hans-peter.steinrueck@fau.de, hubertus.marbach@fau.de

Abstract

We investigated the focused electron beam induced deposition (FEBID) of Ru-containing deposits on SiO$_2$ and sputter-cleaned Si in an ultra-high vacuum. The precursor Ru(CO)$_4$I$_2$ was held at 340 to 345 K, and the applied electron doses were varied from 1.56 to 9.36 C/cm^2, using a focused electron beam (5 keV, 1.5 nA, 10 nm diameter). Local Auger electron spectroscopy (AES) along with subsequent sophisticated fitting procedures not only revealed the elemental composition but also enabled to determine the thickness of the fabricated deposits. Ru contents of up to 60% can be achieved at lower electron doses; at higher doses, the Ru content decreases to 45% and simultaneously the I content increases. The initially lower iodine content is attributed to simultaneous focused electron beam induced etching (FEBIE), which is found to be competing with the deposition process. The etching is evidenced by atomic force

microscopy, where the structures are observed to have negative apparent height for low electron doses. Upon increasing the electron doses, the deposits exhibit positive apparent heights. Hence, the etching is less pronounced at higher electron doses, once the ruthenium surface coverage has increased. The high Ru content and the difficile balance between electron induced deposition and etching considerably expand the possibilities to engineer nanostructured materials.

Introduction

The controlled fabrication of nanostructured material on arbitrary substrates remains challenging in industry and academia. Focused electron beam induced processing (FEBIP), a gas-assisted electron beam lithography method, is a powerful technique to create such nano-scaled structures.[1-3] In the work at hand, FEBIP includes two different techniques, that is, focused electron beam induced etching (FEBIE) and focused electron beam induced deposition (FEBID, also denoted as EBID). FEBIE is the only subtractive method of the latter. Thereby, certain precursor molecules (mostly with halogenides) are locally decomposed yielding reactive fragments, which are suitable to etch the substrate and form corresponding volatile compounds with the latter. In this way FEBIE can effectively etch substrate material locally. In FEBID, the highly focused electron beam of a scanning electron microscope generally in a high vacuum (HV) or more specifically in the study at hand in an ultra-high vacuum (UHV) chamber is used to dissociate adsorbed organometallic precursor molecules. Thereby, the nonvolatile fragments establish a deposit on the substrate while the volatile dissociation products are pumped out from the vacuum chamber. Consequently, the additive fabrication of metallic or metal-containing deposits can be targeted with organometallic precursor compounds.[4-6]

FEBIP methods can be potentially applied to fabricate functional structures like tips for scanning probe microscopy,[7] magnetic logic circuits[8], and single-electron transistors.[9] Furthermore, FEBIP is a state-of-the-art repair method for photolithography masks in the semiconductor industry.[10-11] Beside the obvious advantages of FEBID, there are several challenges, such as the minimum achievable size of deposits (e.g. due to proximity effects[12-14]), reproducibility,[1] and material purity.[7, 15-16] Material purity is one of the most challenging issues. In order to achieve the highest possible purity, the investigation and understanding of the pathways and kinetics of electron-induced precursor dissociation on a particular substrate is mandatory.[5, 17] Gas-phase studies of precursor molecules yield detailed knowledge of the molecule/electron interaction without the influence of the surface. Relevant processes are dissociative electron attachment (DEA), and dissociative ionization (DI).[1, 7, 18-19] In DEA, the

2

precursor molecule is transformed into an excited anion via the attachment of an electron. This excited anion subsequently dissociates into fragments, often via the release of a single ligand from the precursor. In the DI process, the precursor molecule is ionized by electron impact ionization and the resulting cation dissociates into ions and neutrals. The latter process is mostly linked to the release of multiple ligands and represents the primary decomposition and/or deposition of FEBID precursors.[18]

Previous studies reported several suitable organometallic precursors for FEBID yielding deposits with metal contents higher than 60 at.%, such as $Fe(CO)_5$,[20-22] $Co(CO)_3NO$,[23] $Co_2(CO)_8$,[24-25] and $W(CO)_6$.[26-27] However, the majority of deposits achieved via FEBID of organometallic precursors require concurrent or post-deposition purification steps. One particularly interesting class of precursors are Ru-based organometallic compounds, which gain more and more importance regarding the manufacturing of electronic chips,[28] building of interconnect wires,[29] and most importantly for the repair of EUVL masks.[30-32]

There are a few studies addressing Ru-based FEBID processes, which report rather low metal contents of the corresponding deposits in the absence of purification steps. A FEBID study with $Ru_3(CO)_{12}$ addresses the growth rate and the grain size of the obtained structures, but provides no information on the exact content of ruthenium.[33] In another early study, the ratio of ruthenium to carbon of a deposit achieved with $EtCp_2Ru$ as precursor was stated as around 1:9 using energy-dispersive X-ray (EDX) spectra prior to purification. A post-deposition electron beam irradiation of the structures under O_2 atmosphere was performed as a purification method to remove C impurities, but no quantitative information on the atomic composition of purified ruthenium structures was provided. However, the thickness of the deposits was reduced by around 76% after the purification process, indicating that carbon might be "burned off" to some extent.[34]

To address the issue of low Ru content of FEBID structures, a recent study used $(\eta^3\text{-}C_3H_5)Ru(CO)_3Br$ as precursor and applied a gas-assisted purification protocol, that is, annealing the sample in a reducing H_2/N_2 gas atmosphere.[35] The ruthenium content of the as-deposited material was 23 at.% and later on increased to 83 at.% after the described subsequent purification protocol with H_2/N_2. However, this post-deposition treatment has the major drawback of significantly changing the deposit morphology.

A recently published paper reports on gas phase and surface science studies with $Ru(CO)_4I_2$ and $Ru(CO)_4Br_2$ as precursors.[36] The authors examined electron-induced reactions and

performed EBID experiments using a macroscopic electron beam (3 kV, about 1-2 mm diameter spot size). EDX revealed a Ru : Halide (Br, I) ratio of ~1:2. By comparing the reported EDX results with their gas phase results, the authors claimed that there is a correlation between the DEA observed in the gas-phase study and the primary electron-induced decomposition of the ruthenium halide (Br, I) precursors in the non-focused EBID study. Although these precursors yielded promising results, it has been noted in the literature that non-focused electron beam deposition can give quite different results than focused electron beam deposition.[37] However, it is still unclear whether this difference is due to different electron beam parameters or different vacuum conditions.

To prevent unintended effects of purification methods, such as collapse of the deposited structure,[35] an ideal FEBID process would yield pure metallic ruthenium nanostructures. For certain precursors, such as $Fe(CO)_5$ and $Co(CO)_3NO$, FEBID carried out under UHV conditions indeed can yield clean metallic deposits.[20, 23] It has been shown that an autocatalytic growth (AG) process takes place in UHV at room temperature, causing the precursor molecules to dissociate on the initial FEBID deposit upon prolonged precursor dosage such that a clean metallic deposit is formed. In the work at hand, we address one of the most promising ruthenium-based organometallic compounds from literature, $Ru(CO)_4I_2$, using the impact of a tightly focused electron beam from a SEM with the aim to fabricate clean ruthenium depositions in UHV at room temperature without subsequent purification. The quality of the volatile precursor in the gas phase is monitored with quadrupole mass spectrometry (QMS). The quantitative analysis regarding the changes in chemical composition and thickness of FEBID structures is carried out with Auger electron spectroscopy (AES) and scanning Auger microscopy (SAM). Furthermore, we discuss and compare our results with the previously published gas-phase and non-focused EBID studies of the same precursor.

Experimental

Synthesis. $Ru(CO)_4I_2$ was synthesized using a modified literature procedure.[38-40] A solution of $Ru_3(CO)_{12}$ (178.2 mg, 0.2787 mmol, Acros Organics) and hexanes (400 mL) was prepared in a 500 mL Schlenk flask and subsequently purged with hexanes saturated with CO for approximately 10 min. The flask was then irradiated with a blue LED light (450-455 nm, 15 W) while continuing to purge with CO for approximately 20 min until the solution turned clear. The solution was then purged with N_2 in order to remove residual CO and thereafter cooled to

233 K using an acetonitrile dry ice cooling bath. A cooled solution of iodine (246.8 mg, 0.9724 mmol, Scientific) in hexanes (50 mL) was added in one lot to the reaction flask via a syringe, whereupon a yellowish-brown solid immediately precipitated. The solvent was removed under vacuum, leaving a yellow-orange solid which was sublimed at 338 K at 125 mTorr. Crude yield: 208.7 mg, 53.4%. Yield after sublimation: 170.1 mg, 43.6%. The compound was characterized by comparison to literature data.[38-39] IR (hexanes): 2158 (m), 2105 (vs), 2095 (s), 2066 (s) cm^{-1}.

Handling. The $Ru(CO)_4I_2$ precursor was kept at 253 K and filled into a stainless-steel precursor storage holder under nitrogen atmosphere (glove box). The loaded storage holder was then directly attached to the UHV chamber.

Deposition. All structures were fabricated in a modified commercial UHV system (Multiscanlab, Omicron Nanotechnology, Germany) with a base pressure of $p < 2 \times 10^{-10}$ mbar. Mass spectrometry (MS) was performed using a quadrupole mass spectrometer (Pfeiffer / Prisma QMS 200M) for the gas phase $Ru(CO)_4I_2$ precursor with the precursor vessel temperature at 340 K. The UHV system consists of a UHV-compatible electron column (Leo Gemini) for scanning electron microscopy (SEM, nominal resolution better than 3 nm), electron beam-based lithography (EBL, FEBID), local Auger electron spectroscopy (AES), and scanning Auger microscopy (SAM, with a resolution better than 10 nm) using a hemispherical electron energy analyzer. Electron exposures for SEM and lithography were performed at beam energies of 3 and 5 keV, and a beam current of 1.5 nA. The lithographic processes were controlled through a custom-developed software based on LabVIEW 8.6 (National Instruments) and a high-speed DAC PCIe-card (M2i.6021-exp, Spectrum GmbH, Germany).[41] The lithographic parameters were a step size of 6.2 nm and a sweep number of 100. SEM images were acquired at a beam energy of 15 keV and a beam current of 400 pA with SmartSEM (Zeiss). Minor contrast and brightness adjustments were applied. The atomic force microscopy (AFM) experiments were performed with a JPK NanoWizard 4 by using the non-contact mode.

The precursor gas was dosed through a nozzle in close proximity to the sample surface. Based on simulations using GIS Simulator (version 1.5),[42] a factor of 30 was estimated for the local pressure increase on the sample surface compared to the chamber background pressure achieved by using the nozzle. For a precursor chamber pressure of 6.0×10^{-8} mbar, this corresponds to a local pressure at the surface of about 2.0×10^{-7} mbar. The growth regime of the deposits during the FEBID experiments was found in the precursor limited regime (See Supporting Information, Section S1).

Precursor Treatment. Prior to each FEBID experiment, the precursor was exposed to vacuum several times via the turbo pump of the UHV chamber to remove residual gases present in the precursor container. During the purification step, chamber pressure and volatile fragments were observed by ion gauge and MS, respectively. The volatility of the precursor was studied by MS with the precursor container at elevated temperatures. Figure 1 shows the mass spectrum of the $Ru(CO)_4I_2$ precursor at 340 K on a logarithmic scale. The significant peaks are associated with C^+ ($m/z = 12$), O^+ ($m/z = 16$), CO^+/N_2^+ ($m/z = 28$), Ru^+ ($m/z = 97, 100, 101, 102, 103, 105$), and I^+ ($m/z = 128, 129$), indicating that at this temperature $Ru(CO)_4I_2$ is volatile enough to be detected by MS.
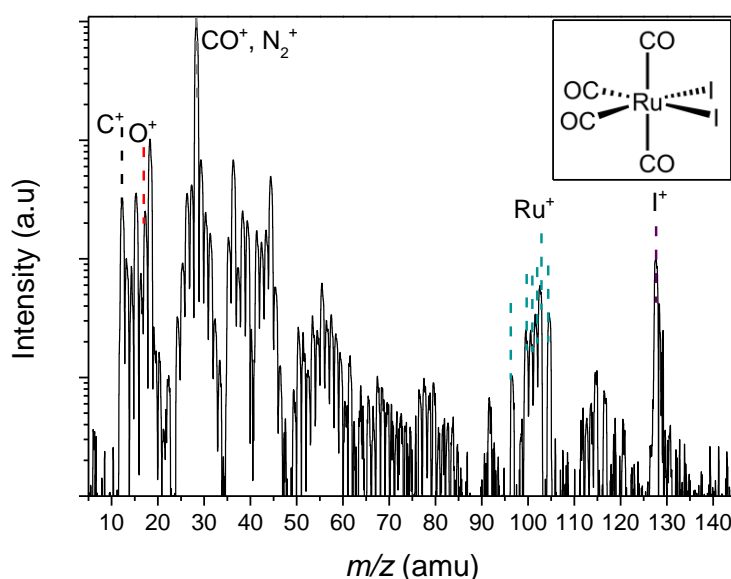

Figure 1. Logarithmic plot of mass spectrum of $Ru(CO)_4I_2$ at a container temperature of 340 K, and a precursor pressure of 4×10^{-8} mbar.

Results and Discussion

The FEBID experiments were carried out on two different substrates, SiO_2 (200 nm) / Si(100) and sputtered clean Si. In a first step, focused electron beam induced deposition experiments were performed on a commercially available SiO_2 (200 nm) / Si(100) substrate kept at room temperature. Before FEBID, no specific preparation was applied to clean the SiO_2 sample. During the FEBID process, the precursor container was heated to a temperature of about 340-345 K to transfer enough volatile gas into the UHV chamber. Different electron doses were applied to study the deposition behavior of the precursor at a chamber pressure of 6×10^{-8} mbar (local pressure at sample: 2.0×10^{-7} mbar; see Experimental). The chamber pressure is about 5

times lower compared to the previously mentioned FEBID studies with $Fe(CO)_5$ and $Co(CO)_3NO$ precursors performed under UHV conditions.[43-44] The comparably low pressures are due to the low vapor pressure of the precursor, and consequently a correspondingly reduced deposition rate is expected. Therefore, a rather low SEM acceleration voltage of 5 keV was selected to increase the secondary electron yield and thus enhance the deposition rate for $Ru(CO)_4I_2$ in the experiments. Using this acceleration voltage, $4 \times 4 \ \mu m^2$ squares were written using a comparably high beam current of 1.5 nA. The fabricated FEBID structures were examined with SEM and AES and partially also with AFM. Figures 2a and 2b depict SEM images of FEBID deposits fabricated with electron exposures of 1.56 and 9.36 C/cm^2, respectively. AES spectra acquired on the bare substrate and on deposited structures are plotted in Figure 2c. On the pristine SiO_2 surface (black spectrum), only two AES signals are visible. The peak at 265 eV and a weak shoulder at 249 eV are attributed to C_{KLL} Auger transitions of carbon in carbidic form,[45] and the peaks at 468, 483, and 503 eV are assigned to O_{KLL} Auger transitions of SiO_2.[46] After deposition with 1.56 C/cm^2, signals at 200, 231, and 273 eV indicative of the Ru_{MNN} transitions[46] are visible, along with the carbidic carbon signal at 249 eV (the C_{KLL} peak at 265 eV is hidden under the Ru peaks).[45] The characteristic (main) I_{MNN} Auger peaks for iodine are observed at 509 and 519 eV.[47] While the latter are barely distinguishable for 1.56 C/cm^2 (red spectrum in Figure 2c), they are clearly visible at higher doses. The increase of a broad and small peak at approximately 420 eV can also be attributed to iodine signals, since three additional iodine transitions have previously been reported for the kinetic energy peak positions at 380, 437 and 446 eV.[46]
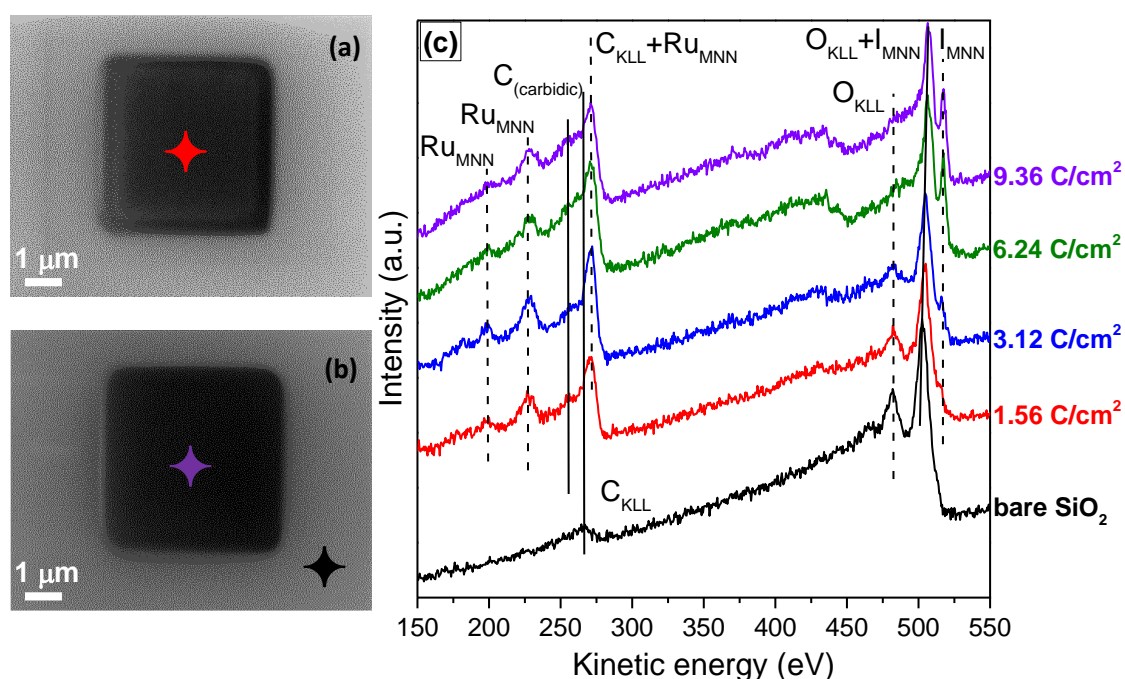
Figure 2. SEM images of the FEBID structures produced by electron dose of 1.56 C/cm^2 in (a) and electron dose of 9.36 C/cm^2 in (b) at electron beam parameters of 5 keV and 1.5 nA. AES spectra from the bare SiO$_2$ surface prior to deposition (black line in (c) and black star on the surface) and the results from FEBID structures prepared using electron doses of up to 9.36 C/cm^2. Colored stars in (a) and (b) indicate the positions where the spectra in (c) where acquired.

Due to the overlap of the Ru$_{MNN}$ with the C$_{KLL}$ signals and the I$_{MNN}$ with the O$_{KLL}$ signals, the AES results were investigated in Figure 3 on an expanded scale. The spectra were grouped separately for the Ru/C (a) and the I/O (b) energy region. The quantitative analysis of the overlapping Auger peaks is not straightforward, and for comparison to literature different relative sensitivity factors (RSFs) have to be considered when different primary electron beam energies are used.[45] Auger spectra are often measured (using lock-in techniques), plotted and analyzed in the differential form, that is dI/dE vs energy (I: intensity, E: kinetic energy), which makes the separation of overlapping peaks very difficult. Our setup allows for directly measuring I(E) with a reasonable signal-to-noise ratio and energy resolution, similar to X-ray photoelectron spectroscopy, which allows for separating overlapping peaks by peak fitting. As a reference for the O$_{KLL}$ and C$_{KLL}$ signals, we used the spectrum of the bare SiO$_2$ substrate with its carbon contamination. A Ru(001) single crystal, cleaned by Ar$^+$ sputtering (Figure S1), served as a reference concerning peak shape, position, and width of the Ru$_{MNN}$ peaks. Its cleanliness was confirmed using a standard procedure, based on the intensity ratio of two peaks in dI/dE spectra at 273 and 231 eV (I$_{273eV}$/I$_{231eV}$). We determined this value to 2.3 after numeric differentiation of our undifferentiated I(E) spectrum (Figure S2). This value agrees very well with literature values from 2.1 to 2.5 for clean Ru(001) surfaces,[46, 48] and, we can thus use the corresponding spectrum as reference for fitting the spectra of our FEBID deposits from Ru(CO)$_4$I$_2$ in Figure 3.

As the first step in the quantitative analysis, a linear background (BG) was subtracted from the spectra. The AES peaks were fitted with multiple peaks using Voigt functions. For the fitting routines, area constraints were applied for the peaks that belong to one element, i.e., fixed ratio for the Ru peaks. The resulting signals are plotted in Figure 3 for the C$_{KLL}$/Ru$_{MNN}$ (a) and O$_{KLL}$/I$_{MNN}$ (b) regions. In line with C$_{KLL}$ peak positions from literature,[45-46] the C$_{KLL}$ region of the bare SiO$_2$ surface in Figure 3a can be fitted with two peaks at 249 and 265 eV (black lines; the orange envelope shows excellent agreement with the data, R$^2 \geq 0.98$). The Ru$_{MNN}$ peaks of the FEBID deposits were fitted based on the peaks of Ru(001) in Figure S2, where five peaks can be clearly identified after fitting (R$^2 = 0.98$) at 184, 200, 215, 230, and 273 eV. The small peaks of the carbon impurities are observed at the exact kinetic energy positions as for the SiO$_2$

substrate. The characteristic Ru_{MNN} peaks for the FEBID deposits (Figure 3a, green lines) exactly match those found in previous studies.[45-46, 49] The O_{KLL} spectrum of the bare SiO_2 substrate was fitted by three peaks 465, 483 and 503 eV, (Figure 3b, red lines; $R^2 \geq 0.98$) in good agreement with literature values.[46, 50] For the FEBID deposits, the most intense peak is found initially at 503 eV, and shows an additional small peak at lower kinetic energy of 495 eV with increased electron doses. The new peak is assigned to the change from the SiO_2 substrate to O signals related to the precursor dissociation products RuO_x. Since the Ru signal has already saturated at the highest dose of 9.36 C/cm^2, we assume that the spectrum is mostly composed of the RuO_x signals plus the partly overlapping iodine signals, both stemming from the formed deposit. We obtain the best fit result with 3 peaks for the oxygen contribution at 495, 485 and 472 eV (blue) and two peaks for the iodine contribution at 509 and 519 eV (purple). The three envelopes of the SiO_2-, RuO_x- and iodine-derived peaks are then used to fit the complete data set.
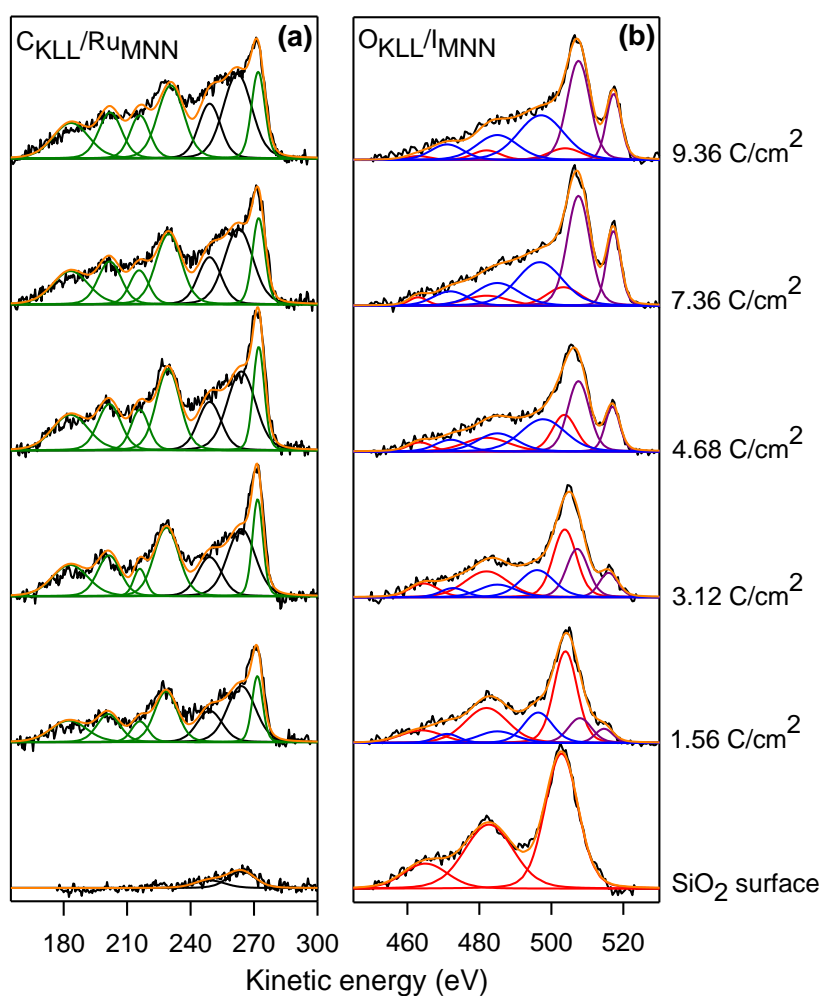
Figure 3. AES spectra of FEBID structures for selected electron doses (5 keV and 1.5 nA) after subtraction of a linear background. (a) C_{KLL}/Ru_{MNN} region, (b) O_{KLL}/I_{MNN} region. Deconvoluted peaks are depicted in green for Ru, black for C, red for surface-related O (SiO_2), blue for deposition-related O (RuO_x), and purple for I. The fit envelopes are shown in orange and the raw signals in black lines. For details of the fitting procedure see text.

The quantitative analysis of the fit results of the Ru, C, O and I Auger signals is shown in Figure 4, using the same color code as in Figure 3. Overall, we find that the Ru signals exhibit the strongest initial increase, while the iodine signal initially increases comparably slow, with carbon and oxygen falling in between. The quantitative analysis of the AES data now allows for determining the composition of the FEBID deposits. Figure 5 depicts the dependence of the atomic concentrations of the different elements for the 4×4 μm^2 FEBID squares deposited with varying electron doses. Atomic concentrations are determined from the spectra in Figure 3, considering AES relative sensitivity factors (RSFs) derived empirically from standard materials,[46] namely 0.35 for the O_{KLL} peak at 495 eV, 0.21 for the I_{MNN} peak at 509 eV. For ruthenium and carbon, the Ru_{MNN} peak at 231 eV and the C_{KLL} peak at 250 eV were used, since these peaks can be best separated from contributions of other elements.[45, 51-52] The corresponding RSFs were calculated separately according to the reference sample standards[46] (see Supporting Information, Figure S3), yielding 0.18 for the C_{KLL} peak at 250 eV and 0.11 for the Ru_{MNN} peak at 231 eV.
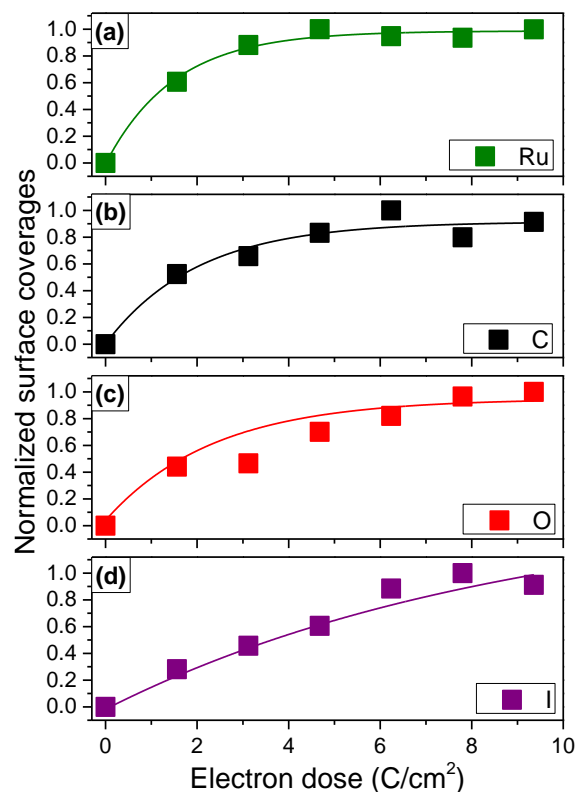
Figure 4. Quantitative analysis of the relative amounts of deposited C, Ru, I, and O as a function of electron dose (C/cm^2); the lines in the graph serve as a guide to the eye.

The FEBID structures produced with electron doses of 1.56 and 3.12 C/cm^2 exhibit compositions with around 60 at.% Ru, 15 at.% I, 15 at.% C and 10 at.% O. Upon increasing the electron dose up to 7.80 C/cm^2, the Ru content decreases by ~15 at.% and the I content increases by ~15 at.%, while C and O contents do not change significantly. The FEBID structure deposited with the highest electron dose of 9.36 C/cm^2 has a composition of around 47 at.% Ru, 25 at.% I, 14 at.% C and 14 at.% O. From the data shown in Figure 5, it is clear that the highest Ru purities are achieved at low electron doses. We will provide a more detailed analysis on this behavior later in the manuscript.
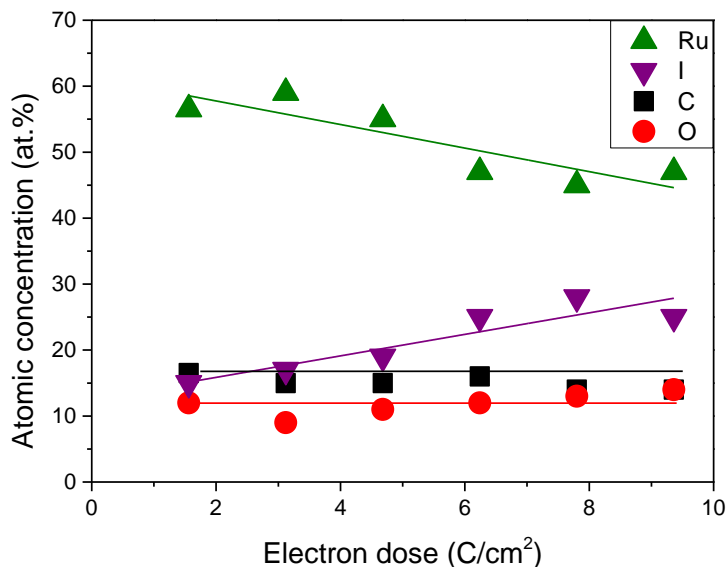
Figure 5. Atomic concentrations (at.%) of the elements in deposited structures created from $Ru(CO)_4I_2$ under different electron doses (5 keV and 1.5 nA), as deduced from Figures 3 and 4. The lines drawn in the figure according to the color of each element are guide to the eye.

In order to obtain complementary information on the deposition process, we investigated the heights of the FEBID deposits on SiO_2 in Figure 2 by non-contact AFM. Figures 6a, 6b, and 6c depict the 2D AFM images, corresponding height profiles, and 3D AFM images for the FEBID structures for the selected electron doses of 1.56 C/cm^2 (green frames and line), 3.12 C/cm^2 (blue), 4.68 C/cm^2 (pink), 7.80 C/cm^2 (purple), respectively. Notably, the line profiles for the small electron doses in Figure 6b reveal that the deposit is actually lower than the surface level (Z = 0 nm) of the substrate. This indicates that initially an etching process occurs along with the deposition process. In Figure 6d, the apparent AFM thickness of the deposits is plotted vs electron dose (orange circles); the data evidence that up to 6.24 C/cm^2 the apparent height is negative and only at high electron doses (≥ 7.80 C/cm^2) a positive apparent height is reached. The detailed analysis of the line profiles in Figure 6b also shows pronounced dips at the edges of the deposits, which are also indicative of etching. The depth of the negative dips is plotted in Figure 6d vs electron dose (open black circles); it changes from -2.8 to -1.3 nm, when the electron dose is increased from 1.56 to 9.36 C/cm^2.

Similar etching effects, showing up as holes at the edges of deposited structures, were also observed by Mulders *et al.*,[53] when using Au(CO)Cl as precursor molecule on SiO_2; they were attributed to the secondary electrons generated by backscattered electrons. To test this hypothesis, we simulated the radial distribution of BSEs versus the number of electrons

impinging on the SiO$_2$ substrate with the CASINO Monte Carlo Program (V2.42),[54] using our experimentally applied parameters (5 keV beam with diameter of 10 nm). The resulting radial distribution is superimposed on top of the enlarged AFM image of Figure 6c (bottom; red-dashed square) in Figure 6e. The width of the etch dip near to the edge of the deposited structure fits very well to the simulated exit radius (~ 0.4 µm) of BSEs.
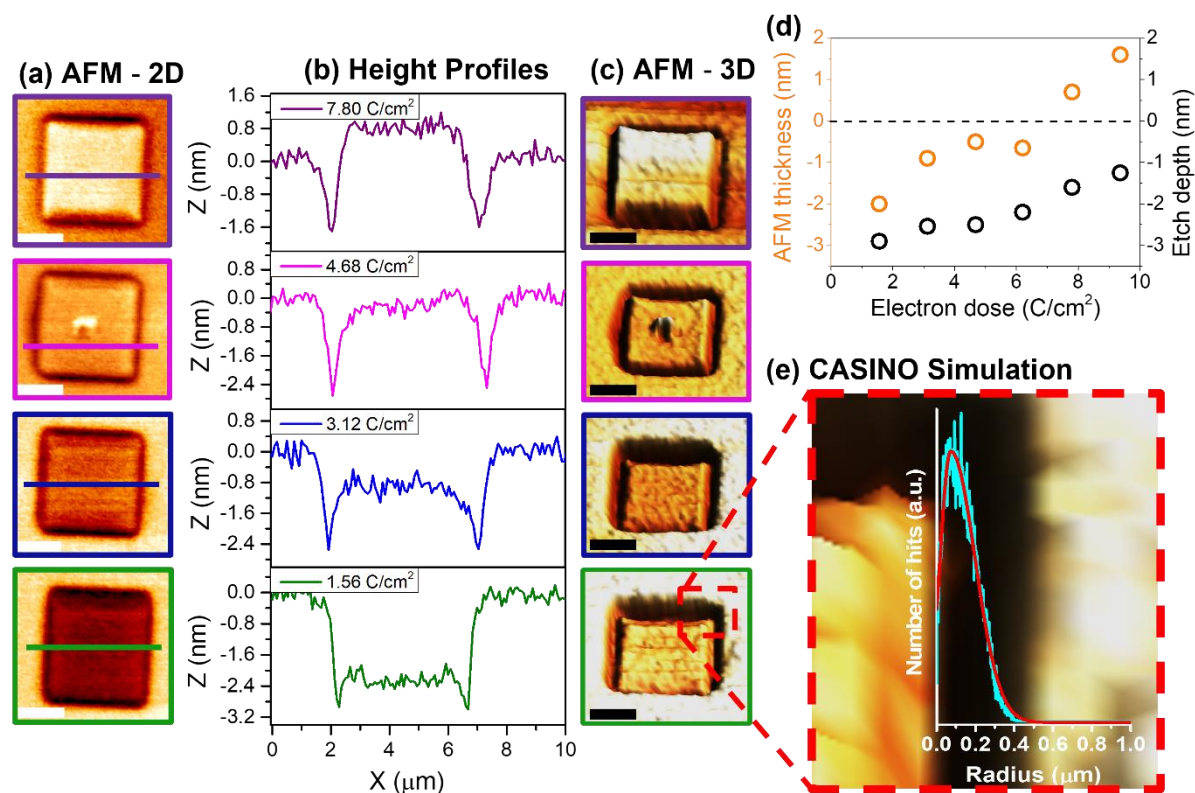
Figure 6. (a) 2D AFM images, (b) corresponding line profiles, and (c) 3D AFM images for the FEBID structures produced with electron doses of 1.56 C/cm^2 (green lines and frames), 3.12 C/cm^2 (blue), 4.68 C/cm^2 (pink) and 7.80 C/cm^2 (purple). (d) Thickness of FEBID structures from AFM versus the height of the negative dips. (e) Magnified AFM image superimposed with the simulation of the BSE exit radius (raw data: cyan; fit: red) obtained with the CASINO Monte Carlo Program.

Etching of the SiO$_2$ substrate and Ru deposition are competing processes. At low electron doses, etching occurs in the directly irradiated square area and in the BSEs exit region (proximity effect area). With increasing dose, Ru deposition in the directly irradiated square seems to occur much faster than in the BSEs exit region (proximity effect area), leading to a decrease of the etching efficiency and the growth of the Ru deposit thickness. This behavior induces the observed etch dips, due to continued etching of the regions. The negative thickness of the square deposits deduced from the AFM line scans at low electron doses (Figures 6b and 6d) demonstrates that etching dominates in this regime and that initially the substrate is etched

faster than the Ru deposition occurs. The situation changes with increasing electron dose (which we achieve by increasing the dwell time). From these observations, we conclude that the deposited Ru is not etched (from a certain thickness on), and thus inhibits further etching of the substrate.

Due to the etching effect, the AFM line scans only provide apparent thicknesses (Figures 6b and 6d). In order to obtain direct and complementary information on the true thickness of the Ru-containing deposits, we measured the attenuation of the Si Auger signal of the underlying substrate as a function of electron dose (these data were not measured for the deposits shown in Figure 2). To be able to directly compare the data, we used the identical electron beam parameters and electron doses as for the structures on SiO_2 shown in Figure 2. The only difference was that we used an oxide-free Si substrate, but we expect no difference in the deposition rate on SiO_2 and clean Si.

The clean Si surface was obtained by sputtering the SiO_2/Si substrate long enough to completely remove the SiO_2 layer (Figure S4) yielding a carbon- and oxygen-free Si surface. The thicknesses of the deposits are determined from the attenuation of the Si_{MNN} Auger signal of the substrate at a kinetic energy of 1615 eV (see Figure S5). Considering its attenuation length (inelastic mean free path) of $\lambda=3.02$ nm and an average emission angle ϑ of 35°, the layer thickness is calculated according to $I=I_0 exp(-d/\lambda(E_B)cos\vartheta)$.

In Figure 7a, the heights obtained from AES on clean Si (full blue circles) are plotted; they show the expected linear increase of the deposit thickness with electron dose as depicted with a blue line. Figure 7a also shows the apparent heights of the FEBID structures on SiO_2 estimated from AFM line scans (open orange circles; same data as in Figure 6d) to compare the overall deposition thicknesses and etch depths. The difference between the expected deposit thickness and apparent heights can be deduced from the differences of the two data sets in Figure 7a, that is, the difference of the AES and AFM heights. The larger difference at small electron doses ($\leq$ 3.12 C/cm^2) indicates that etching dominates as compared to deposition. As the electron dose is increased, deposition becomes dominant, which is reflected in a positive apparent height. The only decisive factor in the competition between etching and deposition is the variation in electron dose. In Figure 7b, the actual changes between the heights obtained from AES and AFM (Δ = AES – AFM) were plotted in the same graph (black squares; right vertical scale) with the Ru surface coverage from Figure 4a (green squares; left vertical scale). From this

figure, it is evident that an increasing Ru surface coverage goes along with reduced etching. Therefore, we conclude that Ru mitigates the FEBIE process.
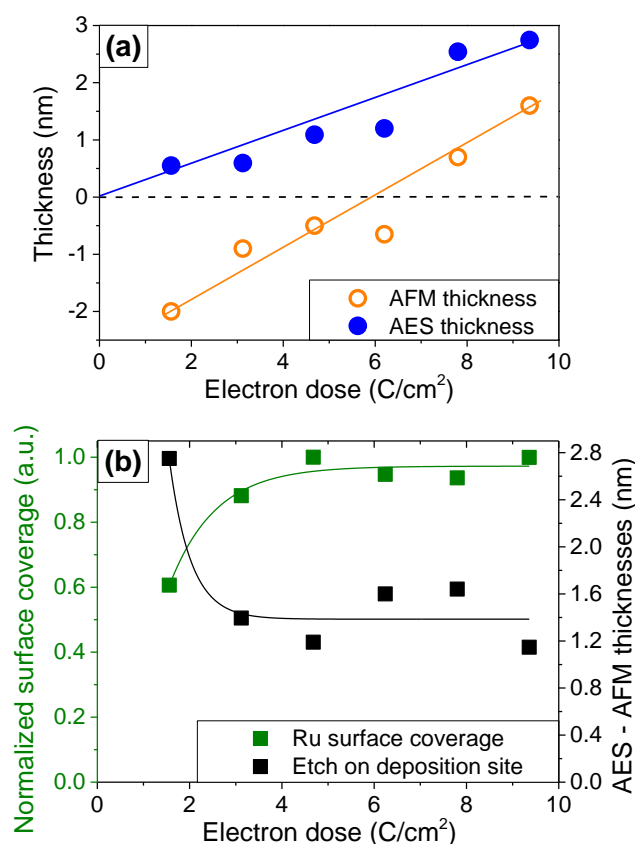
Figure 7. (a) Expected thickness of the FEBID structures vs electron dose obtained from AES (blue full circles) compared to the apparent thickness obtained from AFM line scans (orange open circles). (b) The difference between expected and apparent heights (black full squares) vs electron dose compared with the Ru surface coverage (green full squares) from Figure 4a. The lines depicted in each graph serve as a guide to the eye.

Our results strongly indicate that the focused electron beam induced etching (FEBIE) process is blocked by the FEBID deposits. In previously published papers, FEBIE has been extensively studied and it was proposed that halogen ligands can cause an etching process by forming the volatile by-product under the influence of electron beam. While the existing studies mainly focused on XeF_2 as precursor gas on different substrate materials,[55-58] also Cl_2 was reported to etch a Ge substrate in the presence of an electron beam.[59] The conditions specified in literature for successful FEBIE correspond to those used in our study, namely a low hydrocarbon level in the chamber, along with a focused low-energy high-current electron beam, and short or long dwell times depending on the systems.[58-59] Moreover, the studies combining FEBIE and FEBID typically used two different precursor sources, one for FEBID and one for

FEBIE. The advantage of simultaneous FEBID and FEBIE is an increased metal content of deposited material.[60-62] However, also unintended co-deposition of etching-related material has been reported.[57, 63-64] To overcome this challenge, it appears feasible to use only one precursor source to initiate the competing and simultaneous FEBID and FEBIE processes.

As outlined above, choosing the appropriate experimental conditions is instrumental to obtain the best compromise between etching and deposition. In our study, we used the halide ligand-containing $Ru(CO)_4I_2$ precursor and an electron beam with a diameter of ~10 nm, an energy of 5 keV, and a current of 1.5 nA in UHV. Increasing the electron dose by increasing the dwell time leads to more material deposition, which in turn causes a decrease in the etching effect. Therefore, less etching is expected in the structure produced with the highest electron dose (comparing the Figures 6a, 6b, and 6c).

As a next step, we will evaluate one more route to increase the thickness of the deposit. The thickness is of high relevance for applications; e.g., it has been shown that a 2.5 nm thin Ru capping layer is sufficient to protect Mo-Si EUV reflective mirrors.[30] Apart from applying larger electron doses, reducing the step size or defocusing the beam, one route to increase the growth rate and thus the thickness in FEBID is to decrease primary electron beam energy. The main driver for the increased deposition rate is the increase of the secondary electron yield at lower beam energies.[2] Other options include using a nitrogen co-flow during FEBID,[34] but this is not applicable to our experimental setup.

As shown in Figures 5 and 6, a good balance between the FEBIE and FEBID process might yield a high metallic content in the structures with sufficient thickness. Lowering the electron beam energy can increase the contribution of iodine to the etching process and also increase the thickness of the deposited structure due to the increased secondary electron yield. In this way, it might be possible to establish an optimized balance between etching and deposition rates to obtain high content.

With the goal to increase the thickness of the deposit and of the metallic concentration, we lowered the primary beam energy from 5 to 3 keV. All other parameters such as beam current and electron dose were kept constant. In addition, we used a carbon- and oxygen-free Si surface instead of SiO_2. The SEM image of a 4×4 μm^2 deposit produced by FEBID on this clean Si substrate using a dose of 9.36 C/cm^2 (3 keV, 1.5 nA, container temperature: 345 K), is depicted in Figure 8a, and the corresponding local Auger spectra in Figure 8b. The thicknesses of the deposits obtained with electron beam energies of 5 and 3 keV are determined from the

attenuation of the Si_{MNN} substrate Auger signal at 1615 eV (see Figure S6). For 5 and 3 keV, the Auger signal decreases to 42% and 20% of its original intensity, respectively. From these values, the thicknesses of the layers are calculated as 2-3 and 4-5 nm for 5 and 3 keV, respectively, by considering the previously mentioned attenuation length and average emission angle.

To further characterize the deposit and visually demonstrate the selectivity of the FEBID process, we performed drift-compensated Scanning Auger Microscopy (SAM) at 231 eV. The SAM data in Figure 8c indeed prove the selectivity of the FEBID with $Ru(CO)_4I_2$ on Si and indicate a significant amount of deposited Ru. To obtain the elemental composition, we also performed local Auger spectroscopy on the deposit at the position indicated in Figure 8a. The corresponding spectrum is shown in Figure 8b along with the peak fitting analysis for the Ru/C and I/O regions (as described above). The quantitative analysis of the structure in Figure 8 yields 52 at.% Ru, 22 at.% I, 14 at.% C, and 12 at.% O. Notably, this Ru content for the 3 keV deposit is by 5 at.% larger than the value of 47 at.% for the 5 keV deposit. To the best of our knowledge, the value of 52 at.% is the highest reported value so far without any pre-and/or post-purification methods applied.

The larger Ru content of the structures in Figure 8 as compared to Figure 5 (both for 9.36 C/cm^2) goes along with a decrease in the I and O content by ~3 at.% and ~2 at.%, respectively, which could be related to the balance between FEBIE and FEBID, and also to maintain a clean Si surface before deposition.

When comparing our best FEBID results (52 at.% Ru, 22 at.% I, 14 at.% C, 12 at.% O) to literature results acquired with a non-focused electron beam[36] (31 at.% Ru, 56 at.% I, 8 at.% C, 5 at.% O) using the same precursor molecule under otherwise similar nominal conditions, it is obvious that the lower Ru content (31 at.% vs. 52 at.%) of the literature EBID result goes along with increased concentrations of C, O and in particular I (56 at.% vs. 22 at.%). We speculate that the Ru:I ratio is influenced by the electron beam current density, which is about a factor of 360 larger in our FEBID experiment (300 nA on 20 x 57 μm^2 vs. 1.5 nA on ~15 nm^2), and concurrent iodine-based etching process related to this high current density. At the higher electron current density in FEBID than in EBID, deposited species could be subject to additional electron bombardment, thus removing iodine as etching and desorption products and increasing the metal purity of deposits.
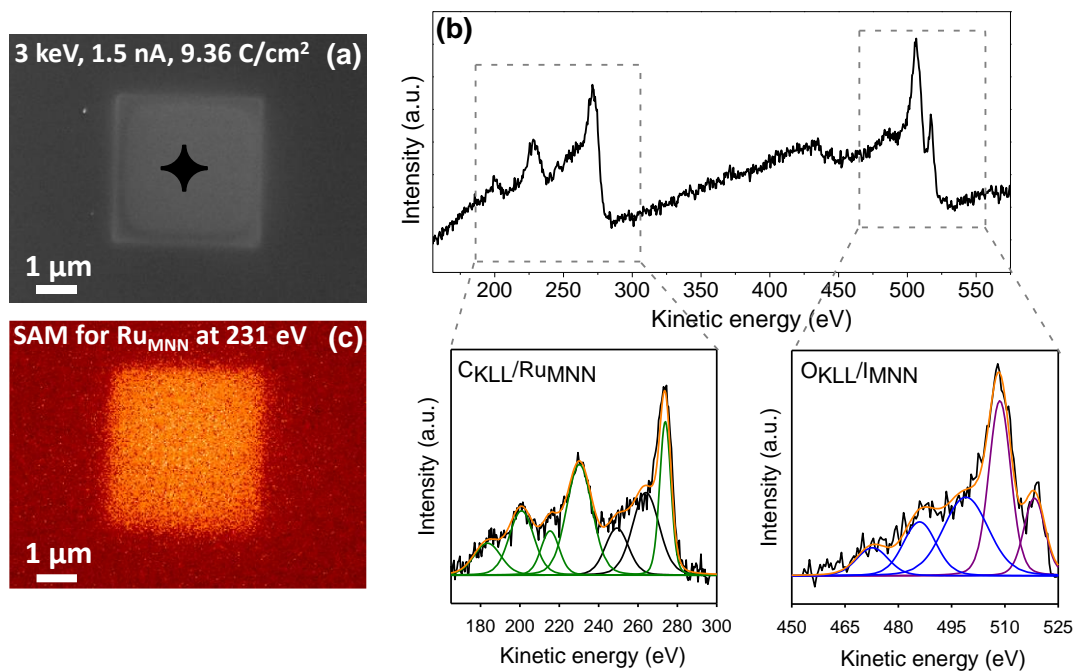
Figure 8. a) SEM image of FEBID structure under an electron dose of 9.36 C/cm^2. The black star represents the point at which spectra were acquired. b) local AES of the deposition from (a) and fitted regions for C_{KLL}/Ru_{MNN} and O_{KLL}/I_{MNN} depicted with dashed grey lines, c) SAM from FEBID structure for the Ru_{MNN} peak at 231 eV.

Finally, we compare the stoichiometry of the deposit with that of the intact precursor $Ru(CO)_4I_2$, which is 14 at.% Ru, 29 at.% I, and 57 at.% C and O. In our study, the Ru content of the FEBID deposits is with 52 at.% much higher than in the precursor. Therefore, we conclude that the tightly focused electron beam leads to the ejection/removal of an average of 3.5 CO ligands and 1.5 I atoms during the balance stage of FEBIE and FEBID. These findings are not much in line with a recently published study comparing gas phase and surface reactions of $Ru(CO)_4I_2$ precursor. Therein, the authors showed that DEA results on average in the loss of 2 CO ligands, and DI results in the loss of an average of 3 CO ligand loss, along with the loss of 0.5 iodine.[36] Therefore, the deposition of the structures from $Ru(CO)_4I_2$ precursor with a highly focused electron beam in UHV might be explained by the contribution of DI and DEA rather than only DEA. However, it should be noted that the experimental conditions in the gas phase study are quite different from those used in FEBID and FEBIE. Hence, the comparison between the gas-phase study and the results achieved have to be treated with caution.

Summary and Conclusion

We prepared Ru-containing deposits on SiO_2/Si and sputtered Si substrates by FEBID in ultrahigh vacuum using $Ru(CO)_4I_2$ as the precursor. The deposition process was performed at comparably low vapor pressure of $Ru(CO)_4I_2$ in the precursor-limited regime, using a 5 or 3 keV focused electron beam with a current of 1.5 nA and a diameter of 10 nm, at electron doses up to 9.36 C/cm^2. The chemical composition and the thickness of the deposits were determined using local Auger spectroscopy. SAM images provide proof for having a selective deposition process with significant amounts of Ru only deposited in the irradiated region. In addition, we also used AFM to obtain complementary information of the shape and thickness of the deposits. Our study reveals that at low electron doses, FEBIE of the SiO_2 substrate by the halide component of the precursor goes along with deposition of a Ru-containing deposit. Since etching dominates in this regime, the deposits show a negative apparent height, as obtained by AFM. At higher doses, that is, when a Ru-containing deposit of a certain thickness has already been formed, the deposit seems to block the etching process and thus yielding an increase in thickness yielding positive apparent heights. The quantitative analysis of the AES results yields the normalized surface coverages of Ru, I, C, and O as a function of electron dose. An initially higher Ru content and lower I content is attributed to the consumption of I in the etching process yielding volatile products. For the higher electron doses, we obtain Ru contents of 45-47 at.% at 5 keV and 1.5 nA, which is significantly higher than reported in the literature so far. This content can be further increased to 52 at.% on Si substrate by lowering the beam energy to 3 keV, while leaving all other parameters constant.

Our investigations demonstrate that due to the competition between FEBID and FEBIE at low electron doses, the deposits have a negative apparent height, that is, significant Ru deposition occurs only after a hole has already been etched into the substrate. What on the first glance might appear as a complication might be exploited for new routes to engineer nanostructure materials. One could envisage that FEBIP might be intentionally stopped at the height of the surface level, resulting in a deposit with high Ru content at the interface of the substrate. Alternatively, a corresponding deposit with negative apparent height could be covered with the substrate material or another material of the right amount using e.g., FEBID, such that a buried Ru deposit is produced with an overall flat surface. This might open the pathway to a new type of three-dimensional nanostructured materials, expanding the applications of buried nanostructures and buried contacts.[65-67] The advantage of the ruthenium carbonyl halide precursor is that it combines the properties for both etching and deposition.

Future studies might reveal additional possibilities to tune the ratio of etching and deposition expanding the technique even more.

Supplementary Materials

Figure S1. AES on Ru crystal before and after sputtering.

Figure S2. AES on clean Ru crystal with E.N(E) vs E and dN/dE vs E signal types.

Figure S3. AES on clean Ag and Ru substrates with E.N(E) vs E and dN/dE vs E signal types.

Figure S4. AES on SiO_2 substrate before and after sputtering.

Figure S5. AES intensities of Si_{MNN} peak (1615 eV) under different electron doses.

Figure S6. AES damping Si_{MNN} signal for clean Si, 5 keV and 3 keV FEBID structures.

Section S1. Calculations for the precursor flux and current density.

References

(1)   Van Dorp, W.; Hagen, C. W., A Critical Literature Review of Focused Electron Beam Induced Deposition. *J. Appl. Phys.* **2008,** *104*, 10.

(2)   Huth, M.; Porrati, F.; Schwalb, C.; Winhold, M.; Sachser, R.; Dukic, M.; Adams, J.; Fantner, G., Focused Electron Beam Induced Deposition: A Perspective. *Beilstein J. Nanotechnol.* **2012,** *3*, 597-619.

(3)   Randolph, S.; Fowlkes, J.; Rack, P., Focused, Nanoscale Electron-Beam-Induced Deposition and Etching. *Crit. Rev. Solid State Mater. Sci.* **2006,** *31*, 55-89.

(4)   Carden, W. G.; Lu, H.; Spencer, J. A.; Fairbrother, D. H.; McElwee-White, L., Mechanism-Based Design of Precursors for Focused Electron Beam-Induced Deposition. *MRS Commun.* **2018,** *8*, 343-357.

(5)   Yu, J.-C.; Abdel-Rahman, M. K.; Fairbrother, D. H.; McElwee-White, L., Charged Particle-Induced Surface Reactions of Organometallic Complexes as a Guide to Precursor

Design for Electron-and Ion-Induced Deposition of Nanostructures. *ACS Appl. Mater. Interfaces* **2021,** *13*, 48333-48348.

(6)   Barth, S.; Huth, M.; Jungwirth, F., Precursors for Direct-Write Nanofabrication With Electrons. *J. Mater. Chem. C* **2020,** *8*, 15884-15919.

(7)   Utke, I.; Hoffmann, P.; Melngailis, J., Gas-Assisted Focused Electron Beam and Ion Beam Processing and Fabrication. *J. Vac. Sci. Technol., B: Microelectron. Nanometer Struct. Process., Meas., Phenom.* **2008,** *26*, 1197-1276.

(8)   Fernández-Pacheco, A.; Serrano-Ramón, L.; Tyliszczak, T.; Chou, K.; Córdoba, R.; Szkudlarek, A.; O'Brien, L.; Kapusta, C.; Ibarra, M.; De Teresa, J., Correlation Between the Magnetic Imaging of Cobalt Nanoconstrictions and Their Magnetoresistance Response. *Nanotechnology* **2012,** *23*, 105703.

(9)   Di Prima, G.; Sachser, R.; Trompenaars, P.; Mulders, H.; Huth, M., Direct-Write Single Electron Transistors by Focused Electron Beam Induced Deposition. *Nano Futures* **2019,** *3*, 025001.

(10)   Edinger, K.; Becht, H.; Bihr, J.; Boegli, V.; Budach, M.; Hofmann, T.; Koops, H. W.; Kuschnerus, P.; Oster, J.; Spies, P., Electron-Beam-Based Photomask Repair. *J. Vac. Sci. Technol., B: Microelectron. Nanometer Struct. Process., Meas., Phenom.* **2004,** *22*, 2902-2906.

(11)   Liang, T.; Frendberg, E.; Lieberman, B.; Stivers, A., Advanced Photolithographic Mask Repair Using Electron Beams. *J. Vac. Sci. Technol., B: Microelectron. Nanometer Struct. Process., Meas., Phenom.* **2005,** *23*, 3101-3105.

(12)   Walz, M.-M.; Vollnhals, F.; Rietzler, F.; Schirmer, M.; Steinrück, H.-P.; Marbach, H., Investigation of Proximity Effects in Electron Microscopy and Lithography. *Appl. Phys. Lett.* **2012,** *100*, 053118.

(13)   Plank, H.; Smith, D. A.; Haber, T.; Rack, P. D.; Hofer, F., Fundamental Proximity Effects in Focused Electron Beam Induced Deposition. *ACS Nano* **2012,** *6*, 286-294.

(14)   Drost, M.; Tu, F.; Berger, L.; Preischl, C.; Zhou, W.; Gliemann, H.; Wöll, C.; Marbach, H., Surface-Anchored Metal–Organic Frameworks as Versatile Resists for Gas-Assisted E-Beam Lithography: Fabrication of Sub-10 Nanometer Structures. *ACS Nano* **2018,** *12*, 3825-3835.

(15)   van Dorp, W., Sub-10 nm Writing: Focused Electron Beam-Induced Deposition in Perspective. *Appl. Phys. A* **2014,** *117*, 1615-1622.

(16)   Huth, M.; Porrati, F.; Dobrovolskiy, O. V., Focused Electron Beam Induced Deposition Meets Materials Science. *Microelectron. Eng.* **2018,** *185*, 9-28.

(17)   Spencer, J. A.; Rosenberg, S. G.; Barclay, M.; Wu, Y.-C.; McElwee-White, L.; Fairbrother, D. H., Understanding the Electron-Stimulated Surface Reactions of Organometallic Complexes to Enable Design of Precursors for Electron Beam-Induced Deposition. *Appl. Phys. A* **2014,** *117*, 1631-1644.

(18)   Thorman, R. M.; TP, R. K.; Fairbrother, D. H.; Ingólfsson, O., The Role of Low-Energy Electrons in Focused Electron Beam Induced Deposition: Four Case Studies of Representative Precursors. *Beilstein J. Nanotechnol.* **2015,** *6*, 1904-1926.

(19)   Böhler, E.; Warneke, J.; Swiderek, P., Control of Chemical Reactions and Synthesis by Low-Energy Electrons. *Chem. Soc. Rev.* **2013,** *42*, 9219-9231.

(20)   Lukasczyk, T.; Schirmer, M.; Steinrück, H. P.; Marbach, H., Electron-Beam-Induced Deposition in Ultrahigh Vacuum: Lithographic Fabrication of Clean Iron Nanostructures. *Small* **2008,** *4*, 841-846.

(21)   Shimojo, M.; Takeguchi, M.; Tanaka, M.; Mitsuishi, K.; Furuya, K., Electron Beam-Induced Deposition Using Iron Carbonyl and The Effects of Heat Treatment on Nanostructure. *Appl. Phys. A* **2004,** *79*, 1869-1872.

(22)   Mitsuishi, K.; Liu, Z.; Shimojo, M.; Han, M.; Furuya, K., Dynamic Profile Calculation of Deposition Resolution by High-Energy Electrons in Electron-Beam-Induced Deposition. *Ultramicroscopy* **2005,** *103*, 17-22.

(23)   Vollnhals, F.; Drost, M.; Tu, F.; Carrasco, E.; Späth, A.; Fink, R. H.; Steinrück, H.-P.; Marbach, H., Electron-Beam Induced Deposition and Autocatalytic Decomposition of $Co(CO)_3NO$. *Beilstein J. Nanotechnol.* **2014,** *5*, 1175-1185.

(24)   De Teresa, J.; Fernández-Pacheco, A.; Córdoba, R.; Serrano-Ramón, L.; Sangiao, S.; Ibarra, M. R., Review of Magnetic Nanostructures Grown by Focused Electron Beam Induced Deposition (FEBID). *J. Phys. D: Appl. Phys.* **2016,** *49*, 243003.

(25)   Utke, I.; Michler, J.; Winkler, R.; Plank, H., Mechanical Properties of 3D Nanostructures Obtained by Focused Electron/Ion Beam-Induced Deposition: A Review. *Micromachines* **2020,** *11*, 397.

(26)   Koops, H.; Weiel, R.; Kern, D.; Baum, T., High-Resolution Electron-Beam Induced Deposition. *J. Vac. Sci. Technol., B: Microelectron. Process. Phenom.* **1988,** *6*, 477-481.

(27)   Wich, T.; Luttermann, T.; Mircea, I., *Computational Methods and Experiments in Materials Characterization III;* , Brebbia, C. A., Mammoli, A. A., Eds.; Wit Press, 2007, Vol. 57, pp 73-82.

(28)   Le, V.-G.; Vu, C.-T.; Shih, Y.-J.; Huang, Y.-H., Highly Efficient Recovery of Ruthenium from Integrated Circuit (IC) Manufacturing Wastewater by Al Reduction and Cementation. *RSC Adv.* **2019,** *9*, 25303-25308.

(29)   Paolillo, S.; Wan, D.; Lazzarino, F.; Rassoul, N.; Piumi, D.; Tőkei, Z., Direct Metal Etch of Ruthenium for Advanced Interconnect. *J. Vac. Sci. Technol., B: Microelectron. Nanometer Struct. Process., Meas., Phenom.* **2018,** *36*, 03E103.

(30)   Yan, P.-y.; Spiller, E.; Mirkarimi, P., Characterization of Ruthenium Thin Films as Capping Layer for Extreme Ultraviolet Lithography Mask Blanks. *J. Vac. Sci. Technol., B: Microelectron. Nanometer Struct. Process., Meas., Phenom.* **2007,** *25*, 1859-1866.

(31)   Slaughter, J.; Schulze, D. W.; Hills, C.; Mirone, A.; Stalio, R.; Watts, R.; Tarrio, C.; Lucatorto, T. B.; Krumrey, M.; Mueller, P., Structure and Performance of Si/Mo Multilayer Mirrors for The Extreme Ultraviolet. *J. Appl. Phys.* **1994,** *76*, 2144-2156.

(32)   Rosen, R. S.; Viliardos, M. A.; Kassner, M.; Stearns, D. G.; Vernon, S. P. In *Thermal Stability of Mo/Si Multilayers*, Proceedings Multilayer Optics for Advanced X-Ray Applications, International Society for Optics and Photonics, Vol. 1547, pp 212-220.

(33)   Scheuer, V.; Koops, H.; Tschudi, T., Electron Beam Decomposition of Carbonyls on Silicon. *Microelectron. Eng.* **1986,** *5*, 423-430.

(34)   Noh, J.-H.; Stanford, M. G.; Lewis, B. B.; Fowlkes, J. D.; Plank, H.; Rack, P., Nanoscale Electron Beam-Induced Deposition and Purification of Ruthenium for Extreme Ultraviolet Lithography Mask Repair. *Appl. Phys. A* **2014,** *117*, 1705-1713.

(35)   Jurczyk, J.; Brewer, C. R.; Hawkins, O. M.; Polyakov, M. N.; Kapusta, C.; McElwee-White, L.; Utke, I., Focused Electron Beam-Induced Deposition and Post-Growth Purification Using the Heteroleptic Ru Complex (η^3-C_3H_5)Ru(CO)$_3$Br. *ACS Appl. Mater. Interfaces* **2019,** *11*, 28164-28171.

(36)   Thorman, R.; Jensen, P. A.; Yu, J.-C.; Matsuda, S. J.; McElwee-White, L.; Ingolfsson, O.; Fairbrother, D. H., Electron-Induced Reactions of Ru(CO)$_4$I$_2$: Gas Phase, Surface, and Electron Beam-Induced Deposition. *J. Phys. Chem. C* **2020,** *124*, 10593-10604.

(37)   Mahgoub, A.; Lu, H.; Thorman, R. M.; Preradovic, K.; McElwee-White, L.; Fairbrother, H.; Hagen, C. W., Electron Beam-Induced Deposition of Platinum from Pt(CO)$_2$Cl$_2$ and Pt(CO)$_2$Br$_2$. *Beilstein J. Nanotechnol.* **2020,** *11*, 1789-1800.

(38)   Calderazzo, F.; L'eplattenier, F., Pentacarbonyls of Ruthenium and Osmium. I. Infrared Spectra and Reactivity. *Inorg. Chem.* **1967,** *6*, 1220-1224.

(39)   Johnson, B.; Johnston, R.; Lewis, J., Chemistry of Polynuclear Compounds. Part XV. Halogenocarbonylruthenium Compounds. *J. Chem. Soc. A* **1969**, 792-797.

(40)   Saha, S.; Captain, B., Synthesis and Structural Characterization of Ruthenium Carbonyl Cluster Complexes Containing Platinum with a Bulky N-Heterocyclic Carbene Ligand. *Inorg. Chem.* **2014,** *53*, 1210-1216.

(41)   Vollnhals, F., Exploring Electron Beam Induced Surface Activation for the Fabrication of well-defined Nanostructures: On the Role of Catalytic Processes, Substrates and Precursors. Ph.D. Dissertation, Friedrich-Alexander-Universität Erlangen, Erlangen, Germany, 2015.

(42)   Friedli, V.; Utke, I., Optimized Molecule Supply from Nozzle-Based Gas Injection Systems for Focused Electron-and Ion-Beam Induced Deposition and Etching: Simulation and Experiment. *J. Phys. D: Appl. Phys.* **2009,** *42*, 125305.

(43)   Schirmer, M.; Walz, M.; Vollnhals, F.; Lukasczyk, T.; Sandmann, A.; Chen, C.; Steinrück, H.; Marbach, H., Electron-Beam-Induced Deposition and Post-Treatment Processes to Locally Generate Clean Titanium Oxide Nanostructures on Si(100). *Nanotechnology* **2011,** *22*, 085301.

(44)   Preischl, C.; Le, L. H.; Bilgilisoy, E.; Vollnhals, F.; Gölzhäuser, A.; Marbach, H., Controlled Electron-Induced Fabrication of Metallic Nanostructures on 1 nm Thick Membranes. *Small* **2020,** *16*, 2003947.

(45)   Van Staden, M.; Roux, J., The Superposition of Carbon and Ruthenium Auger Spectra. *Appl. Surf. Sci.* **1990,** *44*, 259-262.

(46)   Davis, L. E., *Handbook of Auger Electron Spectroscopy*, Physical Electronics Division, 1978.

(47)   Krishnan, G. N.; Wood, B. J.; Cubicciotti, D., Auger Electron Spectroscopy Study of The Chemisorption of Iodine on Zirconium. *J. Electrochem. Soc.* **1980,** *127*, 2738.

(48)   Zei, M., Epitaxial Growth of Ru and Pt on Pt(111) and Ru(0001), Respectively: A Combined AES and RHEED Study. *J. Nanotechnol.* **2010,** *2010*, 1-12.

(49)   Ferrari, P.; Rojas, S.; Diaz-Droguett, D.; Cabrera, A., Evaporation of Low-Vapor Pressure Metals Using a Conventional Mini Electron Beam Evaporator. *Instrum. Sci. Technol.* **2014,** *42*, 142-152.

(50)   Nozoye, H.; Matsumoto, Y.; Onishi, T.; Kondow, T.; Tamaru, K., Origin of The Peak Shapes in The Auger Spectrum of Oxygen ($KL_{2,3}L_{2,3}$) on Molybdenum. *J. Phys. C: Solid State Phys.* **1975,** *8*, 4131.

(51)   Kanjilal, A.; Catalfano, M.; Harilal, S. S.; Hassanein, A.; Rice, B., Tracking Electron-Induced Carbon Contamination and Cleaning of Ru Surfaces by Auger Electron Spectroscopy. *J. Vac. Sci. Technol., A* **2012,** *30*, 041401.

(52)   Kanjilal, A.; Catalfano, M.; Harilal, S.; Hassanein, A.; Rice, B., Time Dependent Changes in Extreme Ultraviolet Reflectivity of Ru Mirrors from Electron-Induced Surface Chemistry. *J. Appl. Phys.* **2012,** *111*, 063518.

(53)   Mulders, J.; Veerhoek, J.; Bosch, E.; Trompenaars, P., Fabrication of Pure Gold Nanostructures by Electron Beam Induced Deposition with Au(CO)Cl Precursor: Deposition Characteristics and Primary Beam Scattering Effects. *J. Phys. D: Appl. Phys.* **2012,** *45*, 475301.

(54)   Drouin, D.; Couture, A. R.; Joly, D.; Tastet, X.; Aimez, V.; Gauvin, R., CASINO V2. 42—A Fast and Easy-To-Use Modeling Tool for Scanning Electron Microscopy and Microanalysis Users. *Scanning* **2007,** *29*, 92-101.

(55)   Martin, A. A.; McCredie, G.; Toth, M., Electron Beam Induced Etching of Carbon. *Appl. Phys. Lett.* **2015,** *107*, 041603.

(56)   Randolph, S.; Toth, M.; Cullen, J.; Chandler, C.; Lobo, C., Kinetics of Gas Mediated Electron Beam Induced Etching. *Appl. Phys. Lett.* **2011,** *99*, 213103.

(57)   Toth, M.; Lobo, C. J.; Hartigan, G.; Ralph Knowles, W., Electron Flux Controlled Switching Between Electron Beam Induced Etching and Deposition. *J. Appl. Phys.* **2007,** *101*, 054309.

(58)   Randolph, S.; Fowlkes, J.; Rack, P., Focused Electron-Beam-Induced Etching of Silicon Dioxide. *J. Appl. Phys.* **2005,** *98*, 034902.

(59)   Shawrav, M.; Gökdeniz, Z.; Wanzenboeck, H.; Taus, P.; Mika, J.; Waid, S.; Bertagnolli, E., Chlorine Based Focused Electron Beam Induced Etching: A Novel Way to Pattern Germanium. *Mater. Sci. Semicond. Process.* **2016,** *42*, 170-173.

(60)   Shawrav, M. M.; Taus, P.; Wanzenboeck, H. D.; Schinnerl, M.; Stöger-Pollach, M.; Schwarz, S.; Steiger-Thirsfeld, A.; Bertagnolli, E., Highly Conductive and Pure Gold Nanostructures Grown by Electron Beam Induced Deposition. *Sci. Rep.* **2016,** *6*, 1-10.

(61)   Perentes, A.; Hoffmann, P., Oxygen Assisted Focused Electron Beam Induced Deposition of Si-Containing Materials: Growth Dynamics. *J. Vac. Sci. Technol., B: Microelectron. Nanometer Struct. Process., Meas., Phenom.* **2007,** *25*, 2233-2238.

(62)   Toth, M.; Lobo, C.; Friedli, V.; Szkudlarek, A.; Utke, I., Continuum Models of Focused Electron Beam Induced Processing. *Beilstein J. Nanotechnol.* **2015,** *6*, 1518-1540.

(63)   Lobo, C. J.; Martin, A.; Phillips, M. R.; Toth, M., Electron Beam Induced Chemical Dry Etching and Imaging in Gaseous NH_3 Environments. *Nanotechnology* **2012,** *23*, 375302.

(64)   Toth, M.; Lobo, C. J.; Lysaght, M. J.; Vladár, A. E.; Postek, M. T., Contamination-Free Imaging by Electron Induced Carbon Volatilization in Environmental Scanning Electron Microscopy. *J. Appl. Phys.* **2009,** *106*, 034306.

(65)   Jensen, J. A.; Møller, P.; Bruton, T.; Mason, N.; Russell, R.; Hadley, J.; Verhoeven, P.; Matthewson, A., Electrochemical Deposition of Buried Contacts in High-Efficiency Crystalline Silicon Photovoltaic Cells. *J. Electrochem. Soc.* **2002,** *150*, G49.

(66)   Ali, R.; Saleem, M. R.; Roussey, M.; Turunen, J.; Honkanen, S., Fabrication of Buried Nanostructures by Atomic Layer Deposition. *Sci. Rep.* **2018,** *8*, 1-10.

(67)   Gramse, G.; Kölker, A.; Lim, T.; Stock, T. J.; Solanki, H.; Schofield, S. R.; Brinciotti, E.; Aeppli, G.; Kienberger, F.; Curson, N. J., Nondestructive Imaging of Atomically Thin Nanostructures Buried in Silicon. *Sci. Adv.* **2017,** *3*, e1602586.

For Table of Contents Only: